Hierarchical conformal coating enables highly stable microparticle Si anodes for advanced Li-ion batteries

Yaxiong Yang[a], Shugang Liu[a], Zhe Dong[b], Zhenguo Huang[c], Cheng Lu[d], Yongjun Wu[b], Mingxia Gao[b], Yongfeng Liu[a,b]*, and Hongge Pan[a,b]*

[a]Institute of Science and Technology for New Energy, Xi'an Technological University, Xi'an 710021, China

[b]State Key Laboratory of Silicon Materials and School of Materials Science and Engineering, Zhejiang University, Hangzhou 310027, China.

[c]School of Civil & Environmental Engineering, University of Technology Sydney, 81 Broadway, Ultimo, NSW 2007, Australia.

[d]Zhejiang Institute of Product Quality and Safety Science, Hangzhou 310018, China.

E-mail: mselyf@zju.edu.cn (Y.F.L.), hgpan@zju.edu.cn (H.G.P.)

Abstract:

Microsized silicon powders have great potential for high capacity anode materials in next-generation lithium ion batteries, because of the high gravimetric and volumetric energy densities, ease of mass production and low costs. However, large volume change and consequently rapid capacity fading upon lithiation and delithiation prevent its practical applications. Herein, we demonstrate an effective hierarchical conformal coating strategy for high-performance microsized Si anodes. The Si-based composites consist of an amorphous Li-Si-O inner coating layer and a graphene outer encapsulation layer, which are prepared by coupling reactive milling with electrostatic self-assembly. This unique hierarchical conformal

coating structure not only strengthens the mechanical property (31.8 GPa for the elastic modulus) and promotes the ionic diffusion (2.03×10^{-10} cm^2 s^{-1}) of Si anode, but also effectively stabilizes the electrode/electrolyte interfaces and increases the electronic conductivity. As a result, a high reversible capacity (1450 mA·h g^{-1} at 0.1 A g^{-1}), good cycling stability (97.7% of capacity retention from the 2nd to the 310th cycle at 0.5 A g^{-1}), and high rate capability (703 mA·h g^{-1} at 5 A g^{-1}) have been successfully achieved. These findings provide new insights into the improvement of electrochemical properties of microsized Si composite anodes for high-performance Li-ion batteries.

Keywords: lithium ion batteries, anode materials, silicon, microparticles, hierarchical conformal coating

1. Introduction

The development of rechargeable secondary batteries and corresponding electrode materials with higher specific capacity, longer lifespan, better rate capability and safety is vital for meeting the pressing need of emerging energy-driven technologies [1-9]. As for next-generation Li-ion batteries (LIBs), silicon (Si) has been considered as one of the most promising anode candidates because of its ultrahigh theoretical specific capacity (3578 mAh g^{-1} for $Li_{15}Si_4$ at room temperature), low average voltage (~0.37 V *vs.* Li/Li^+), natural abundance, and environmental friendliness [10-13]. However, the large volume changes (> 300 %) of Si anodes upon lithiation and delithiation give rise to severe pulverization, leading to poor mechanical and electrical contacts, unstable solid-electrolyte interphases (SEIs), and eventually fast capacity decay [14-19]. Reducing particle size of Si-based anode materials to the nanoscale, in the form of nanospheres, nanotubes, nanosheets and nanocrystals, can enhance the mechanical integrity since these strucutres can accommodate the mechanical strain originates from the

repeated volume expansion and contraction, and therefore improve cycling performance [15-20]. However, nanostructured Si anode also brings along new challenges, including uncontrollable side reactions caused by high specific surface area, complex fabrication process and high costs [12,21]. In this regard, microparticle Si should be more promising as practical electrode materials for industrial applications because of their low cost and mass product. Considerable effort has been devoted to designing and developing microsized Si anodes featuring long-term cyclability and rate capability, espeically porous Si, graphene-coated Si, and Si-C composites [21-24], but their fabrication normally rely on toxic chemicals (e.g. hydrofluoric acid (HF)) and involves complicated procedures.

Recently, surface engineering has proven very effective in improving the electrochemical performance of Si nanoparticle anodes, by suppressing the volume expansion upon lithiation and alleviating the adverse side reactions, and has therefore attracted growing attention [25-32]. A wide variety of coatings, including carbon, titanium dioxide, aluminium oxide, silicon oxide, zinc oxide, lithium titanate, silicon oxycarbide, organic polymers have been studied [25-36]. For example, Park *et al*. demonstrated amorphous SiO_x-coated Si nanocomposite anodes with a capacity as high as 1914 mAh g^{-1} and a stable cyclability over 100 cycles [27]. Jiang *et al*. reported that amorphous SiOC-coated Si nanoparticle anodes retained >1030 mAh g^{-1} of capacity over 500 cycles [28]. Similar performance was also obtained by coating PANI and TiO_2 [31]. With the protection of lithium phosphorus oxynitride layer, Si nanofilm anodes delivered ~1200 mAh g^{-1} while cycling at 2.0 A g^{-1} for 1000 times [32]. Silicon nanoparticles encapsulated in multifunctional crosslinked nanosilica/carbon hybrid matrix (Si@n-SiO_2/C) composites maintained 800.7 mAh g^{-1} of capacity after 300 cycles at 1 A g^{-1} [33]. Graphite@Si encapsulated in a carbon conformally coated tiny SiO_2 nanoparticle matrix (G@Si/SiO_2 NPs/C) even contributed to 92% retention after 800 cycles at a 0.5 A g^{-1} with 894 mAh g^{-1} of capacity [34]. However, most of the reported studies focus on nanosized Si anodes, which were processing difficulties as well as high fabrication costs [21]. More importantly, these thin

coatings were not equally effective for microsized Si anodes because of their insufficient mechanical properties [35-38]. To address this issue, we developed a dispersion-strengthened microparticle Si composite, in which polycrystalline Si microparticles were coated by an amorphous SiOC layer strengthened by dispersed SiC and Li_2SiO_3 nanocrystals [38]. Indeed, such a robust coating layer enabled long-term cyclability of microsized Si anode with a high capacity of 957 mA h g^{-1} after 400 cycles at 100 mA g^{-1}. Unfortunately, this oxide coating layer offeres a low electron conductivity, and therefore contributes to an unsatisfactory rate capability (895 mA h g^{-1} at 1 A g^{-1}) [38]. As a result, it is critical to fabricate multifunctional coatings with good mechanical and chemical stability as well as high electron conducting property in order to achieve simultaneously high capacity, long life and fast kinetics, which is highly desirable for next-generation LIBs [39-42].

Building on the previous work on ball-milling derived coating, herein, we demonstrate a composite featuring hierarchical conformal coating over microsized Si that exhibits superior overall electrochemical peformance as LIB anodes. By mechanical ball milling prelithiated commercial microsized Si under O_2 followed by electrostatic self-assembly with reduced graphene oxide (rGO), a composite with pancake-like hierarchical conformal coating was obtained, composing of an amorphous Li-Si-O conformal inner coating layer and a graphene outer encapsulation layer, denoted as Si@Li-Si-O@rGO. Benefiting from the good mechanical strength and high conductivity, the Si@Li-Si-O@rGO composite anode fabricated without additional conductive agent delivers 1450 mA·h g^{-1} of specific capacity at 0.1 A g^{-1}, 97.7% of capacity retention after 310 cycles at 0.5 mA g^{-1} (referred to the 2nd cycle) and 703 mA·h g^{-1} of rate capability at 5 A g^{-1}, superior to the anodes with only Li-Si-O coating or graphene alone. This finding provides new insights into further improvement of overall properties of microsized Si anodes and opens up opportunities for their practical application in high-performance LIBs.

2. Experimental section

2.1 Material Synthesis

Synthesis of Si@Li-Si-O. Commercial Si microparticles (diameters: 1–3 μm, purity: 99.9%, Shanghai ST-NANO, China) were first chemically lithiated by reacting with LiH (purity: 98%, Alfa Aesar, USA) at a molar ratio of 7:2, as described in our previous work [38]. The prelithiated Si was then mechanically milled under 3 bar O_2 (purity: 99.9%, Jingong Materials, China) for 1, 6, 12 and 16 h, respectively, using a planetary ball mill (QM-3SP4, Nanjing, China) at 400 rpm. In each experiment, approximately 1 g of the prelithiated sample and 80 g of stainless steel balls were loaded into a custom-designed milling jar. For comparison, the pristine Si was also milled under 3 bar O_2 for 12h. The handling of LiH and prelithiated Si samples were conducted in a glove box (MBRAUN 200B, Germany) filled with pure argon (H_2O < 1 ppm; O_2 < 1 ppm). Synthesis of Si@Li-Si-O@rGO. The post-12 h milled samples were dispersed in a polyethyleneimine (PEI, purity: 99%, Aladdin, China) aqueous solution (1 mg/mL) to introduce positive charges on the surfaces. After stirring and sonicating for 30 min, solid sample was collected by centrifugating and then washed twice with deionized water. Subsequently, the sample was dispersed in graphene oxide (GO) aqueous solution (1 mg/mL) with further stirring and sonicating for another 30 min. The homogeneous aqueous dispersion was frozen quickly with liquid nitrogen and then transferred to a BIOCOOL Fd-1B-80 freeze-dryer (China) to dry at -50 °C under vacuum. Finally, the sample was heated in a tube furnace at 500 °C for 2 h under Ar to produce the resulting Si@Li-Si-O@rGO composite.

2.2 Characterization

A MiniFlex 600 X-ray diffractometer (Rigaku, Japan) with Cu K_α radiation was used to perform X-ray diffraction (XRD) analysis. XRD data were collected between the scattering angles 2θ of 10° and 90° in a 0.02° increment. A Bruker Tensor 27 unit (Germany) was used to acquire fourier transform infrared (FTIR) spectra in the transmission mode. The tested sample was first mixed with potassium bromide (KBr) at a 1:100 weight ratio and then cold-pressed to form a pellet. A Renishaw Via-Reflex confocal Raman microscope (UK) was used to record

Raman spectra using a laser excitation wavelength of 532 nm. An ESCALAB 250Xi system (Thermo Scientific, USA) with Al K_α radiation was used to perform X-ray photoelectron spectroscopy (XPS) analysis. The results were calibrated using the adventitious C 1s peak centred at 284.8 eV as the reference. The depth profiles of elemental distribution were obtained by Ar^+ sputtering a spot with a diameter of Φ2.5 mm on the sample surface at 15 kV and 10 mA for 10 and 30 min, respectively. A Hitachi-S4800 microscope (Japan) and a FEI Tecnai G2 F20 S-TWIN instrument (USA) were used to carry out scanning electron microscopy (SEM) and transmission electron microscopy (TEM) observations, respectively. A FEI Titan G^2 80-200 Chemi scanning transmission electron microscope was employed to obtain annular dark field STEM images at an acceleration voltage of 200 kV. An energy dispersive X-ray spectroscopy (EDS) mapping was employed to identify the distributions of Si, O, and C elements in the samples. A BT-2003 laser particle size analyser (Baxter instrument, China) was used to examine the size distribution of Si microparticles. A Nano Indenter G200 unit was used to conduct nanoindentation experiments with a continuous stiffness measurement technique. All powder samples were cold-pressed at 15 MPa to form 150 μm thick pellets which were then attached to a stainless-steel substrate. A Vario Micro Elementar Analysensysteme instrument (Germany) was used to analyse C content by heating the sample to 1000 °C under high-purity O_2 atmosphere. A Malvern Zetasizer Nano ZS90 was used to test the Zeta potential of samples.

2.3 Electrochemical measurements

The electrochemical performance of the hierarchically coated micro-sized Si composites was evaluated by assembling 2025 coin-type half-cells at temperatures of 26 ± 1 °C. The prepared Si composites were used as the working electrode, and lithium foil as the counter/reference electrode. Here, a typical slurry method was used to fabricate the working electrodes with 13 mm in diameter. The mass ratio of rGO-free active materials, acetylene black (conducting agent), and sodium alginate (binder) is 7:2:1, while it is 8:2 for the rGO-containing active materials and sodium alginate without additional conducting agent. The slurry was pasted

onto copper foils and dried under vacuum in an oven at 120 °C for 12 h. The loading of active materials was 1.0 ~ 1.2 mg cm^{-2}. The electrolyte was prepared by dissolving 1 M $LiPF_6$ solution in a 1:1:1 (v/v/v) mixture of ethylene carbonate/diethyl carbonate/dimethyl carbonate (EC/DEC/DMC) with 1 vol% fluoroethylene carbonate (FEC) solution as the additive. The cells were assembled in an argon-filled glove box (H_2O < 1 ppm.; O_2 < 1 ppm.). A Neware battery test system (CT-4008, Shenzhen, China) was used to perform galvanostatic charge-discharge cycling experiments in the potential range between 0.01 and 1.5 V (vs. Li^+/Li) at various current densities. The specific capacities were calculated by taking into account the total mass of active materials. An Arbin potentiostat (BT-2000, USA) was used to conduct cyclic voltammogram (CV) measurements in the potential range of 0.01–1.5 V (vs. Li^+/Li) at a scanning rate of 0.1 mV s^{-1}. An Ivium Vertex electrochemical workstation (The Netherlands) was employed to record electrochemical impedance spectra (EIS) at a voltage amplitude of 5 mV in the frequency range of 100 kHz – 10 mHz. The Si@Li-Si-O@rGO||$Li_{1.2}Ni_{0.13}Co_{0.13}Mn_{0.54}O_2$ full cells were assembled and measured at 2.5 ~ 4.2 V. The mass ratio of active materials for the anode to the cathode was carefully balanced and set at 1:12.

3. Results and Discussion

Fig. 1 illustrates schematically the preparation of the composite. First, crystalline Si microparticles (~ 2.5 μm in particle size, Fig. S1a,b) were partially prelithiated by chemically reacting with LiH upon heating. $Li_{12}Si_7$ was clearly identified by XRD (Fig. S1c) and XPS (Fig. S1d) on the surface after the reaction [38]. The prelithiated Si microparticles (~ 1 g) were then loaded into a milling jar filled with 3 bar O_2 and milled at 25 °C. The milling durations were set at 1 h, 6 h, 12 h and 16 h, and the samples obtained were denoted as BM1h, BM6h, BM12h and BM16h, respectively. As the milling time increased, O_2 was gradually consumed (Fig. S2), as evidenced by the invisible XRD peaks associated with $Li_{12}Si_7$ and appearance of peaks due to Li_2SiO_3 (Fig. 2a). The Si and Li_2SiO_3 diffraction peaks then gradually weakened and

broadened with further milling, indicating a gradual decrease in the particle/grain sizes and even amorphization. With Debye-Scherrer equation, the grain sizes of Si and Li_2SiO_3 were quantitatively calculated and they were 22.9 and 6.9 nm, respectively, for the BM16h sample, largely smaller than those of the BM1h sample (44.1 and 17.8 nm) (Fig. S3). Moreover, a bump centred at $2\theta = 25°$ was detected in the XRD patterns, especially for the 16 h-milled sample, which likely originates from amorphous SiO_x [43]. FTIR examinations (Fig. 2b) also indicate the presence of SiO_x because the characteristic absorption bands of the Si-O at 1068 and 470 cm^{-1} intensified with milling time [43,44]. Similar phenomenon was observed in the XPS spectra (Fig. 2c), where the intensity of the Si^{3+} XPS peak at around 102.2 eV, assignable to SiO_x, gradually increased with the milling time [44]. In contrast, the 2p XPS peak of Si^0 at 98.6 eV became much weaker. The weight contents of oxygen were determined to be approximately 2.6%, 24.5%, 24.9%, 25.9%, and 27.2% for pristine Si and post-milled samples (BM1h, BM6h, BM12h and BM16h), respectively. These results indicate that mechanical milling led to reactions between $Li_{12}Si_7$/Si on the surface and O_2 (Equation 1), resulting in conformal coating layer of Li_2SiO_3/SiO_x on the surface of Si microparticles.

$$\frac{1}{6}Li_{12}Si_7 + \frac{5}{6}Si + \frac{3+x}{2}O_2 \xrightarrow{BM} Li_2SiO_3 + SiO_x \quad (1)$$

SEM observation (Fig. 2d-g) showed that after 12 h of ball milling, the particles became spherical in shape. The average particle sizes were determined to be approximately 1.2 μm by means of laser size analysis (Fig. S4), which remained nearly the same after further milling for another 4 h. Subsequently, the BM12h sample was selected as a representative example for TEM observation and selected area electron diffraction (SAED) analyses. Different from pristine Si (Fig. S5a-c), where the typical diffraction pattern of only crystalline Si was observed, three types of diffraction rings, including polycrystalline rings, dotted rings and halo rings, were detected in the SAED pattern of the BM12 sample (Fig. S5d,e), which can be indexed to cubic Si, orthorhombic Li_2SiO_3, and amorphous phases, respectively. The high-resolution TEM image (Fig. 2h) displays a nanocrystalline Li_2SiO_3-containing amorphous layer on the

polycrystalline Si surface. The Li_2SiO_3 nanocrystals with sizes around 8 nm are well dispersed in the amorphous matrix. Here, the measured crystallite size matches with the result calculated by Debye-Scherrer equation (7.7 nm) as shown in Fig. S3. The EDS mapping results (Fig. 2i) reveal a good conformal coating on the surface of Si particles. The coating layer is believed to be composed mainly of SiO_x because of the higher O concentration at the surface, as evidenced by the XPS spectra. The characteristic peak of Si-Si bonding at 518 cm^{-1} in Raman spectra still preserved in spite of the reduced intensities with milling time (Fig. S6). These observations indicate that through mechanical milling the prelithiated Si microparticles under O_2, a nanocrystalline Li_2SiO_3-embeded amorphous SiO_x layer was conformally coated on the surface of Si microparticles, which is denoted as Si@Li-Si-O hereinafter.

The Si@Li-Si-O composites were first assembled into 2025 coin-type half cells to evaluate its performance as LIB anodes. The results display very similar lithiation/delithiation behaviors to well-studied crystalline Si [45], because lithiation occurs at ~0.1 V and delithiation at ~0.43 V (Fig. S7a). The longer ball milling decreased the specific electrochemical capacity but dramatically improved the cyclability, possibly due to the formation of more Li-Si-O layer. The graphene-free Si@Li-Si-O sample obtained by 12 h ball milling delivered the best overall electrochemical properties with 1708 mAh g^{-1} of specific capacity at 0.1 A g^{-1} and 80% of initial coulombic efficiency (Fig. S7b, Table S1). But its capacity retention was measured to be only 68% after 100 cycles at 0.1 A g^{-1} (Fig. S7b, Table S1) and the specific capacity was reduced to 1558 mAh g^{-1} at 0.3 A g^{-1} upon cycling (Fig. S7c,d), indicating a slightly poor rate capability and cycling stability possibly due to the low conductivity and the insufficient mechanical strength of Li-Si-O coating layer [46]. To address these issues, graphene was introduced because of its unique physical and chemical properties, including high electrical conductivity, good mechanical flexibility, superior chemical and thermal stability and large specific surface area [47,48]. A new graphene-encapsulated Si@Li-Si-O composite was fabricated through electrostatic self-assembly encapsulation followed by high-temperature reduction. The Si@Li-

Si-O microparticles was first modified by adsorbing PEI on the surface via electrostatic attraction (Si@Li-Si-O-PEI), which changed the surface charge from negative to positive. Si@Li-Si-O-PEI microparticles were then covered by negatively charged GO via electrostatic attraction (Si@Li-Si-O@GO). The aqueous suspension was freeze-dried and then heated to 500 °C for thermal reduction of GO to obtain Si@Li-Si-O@rGO.

The resulting samples were subjected to structural and composition characterization by XRD, XPS, Raman, SEM, TEM, SAED and EDS. The high-resolution C1s XPS spectra (Fig. 3a) indicated the largely reduced relative intensities of C-O and C=O bonds at 285.6 and 286.7 eV [49], respectively, and the C-C bond at 283.8 eV became dominant after thermal reduction at 500 °C, indicating the successful conversion from GO to rGO. Raman results (Fig. 3b) show the change in the relative intensities of D band (1345 cm^{-1}) and G band (1585 cm^{-1}) and the I_D/I_G ratio was determined to be 0.68 for Si@Li-Si-O@rGO, which is consistent with graphene [49,50]. A small amount of SiC phase was identified in the XRD pattern (Fig. S8), indicating a quite good contact between Si@Li-Si-O and rGO [51]. Low magnification SEM image of the resulting Si@Li-Si-O@rGO (Fig. 3c) shows the typical flake-like morphology. Further high magnification observation (Fig. 3d) indicates very good conformal encapsulation of Si microparticles in graphene (Fig. 3e). TEM images and corresponding EDS mapping confirm the pancake-like hierarchical coating structure for Si@Li-Si-O@rGO. As shown in Fig. 3f, microsized Si particles coated conformally with nanocrystalline Li_2SiO_3-containing amorphous SiO_x layer are well encapsulated in graphene sheets. Here, the fact that the Li 1s XPS peak assignable to Li_2SiO_3 was detected at 54.9 eV (Fig. S9) confirms the presence of nanocrystalline Li_2SiO_3 as mentioned above [52]. Further SAED analyses clearly identified the existence of crystalline Si, Li_2SiO_3, amorphous species and graphene (Fig. S10). Moreover, it should be mentioned that the relative content of graphene in the resulting Si@Li-Si-O@rGO sample was determined to be only 5.2 wt%, lower than most of the reported graphene-modified Si composite anodes (Fig. S11a).

Fig. 4 compares the electrochemical performance of the pristine Si microparticles, Si@Li-Si-O and Si@Li-Si-O@rGO. These three samples display typical lithiation/delithiation behaviors of crystalline Si, as indicated by the CV curves in Fig. 4a, revealing that Si is the primary Li storage active species. The reduced intensities of cathodic and anodic current peaks reveal a decrease in the available Li storage capacity for the composite anodes. This is further confirmed by galvanostatic charge/discharge measurement at 0.01-1.5 V (*vs.* Li/Li^+) and 0.1 A g^{-1} (Fig. 4b). Their initial discharge/charge capacities were determined to be 3517/3009, 2128/1708 and 1884/1450 mAh g^{-1} for the pristine Si, Si@Li-Si-O and Si@Li-Si-O@rGO anodes, respectively. For the Si@Li-Si-O sample, the reduced specific capacity is mainly attributed to the formation of SiO_x and inactive Li_2SiO_3. For the Si@Li-Si-O@rGO anode, the further reduction in the specific capacity is related to the formation of inactive SiC as described above (Fig. S8). Moreover, the formation of SiO*x*, Li_2SiO_3 and SiC were also responsible for the slightly reduced initial coulombic efficiency of the Si@Li-Si-O@rGO anode (ICE: 77%), which is expected to solve thorough the pre-lithiation approach [33]. But the composite anodes demonstrated much improved cycling stability (Fig. 4c). After 100 cycles at 0.1 A g^{-1}, the reversible specific capacity was measured to be 1285 mAh g^{-1} for the Si@Li-Si-O@rGO anodes, corresponding to approximately 89% of capacity retention, which is remarkably higher than those of pristine Si (11%) and Si@Li-Si-O (68%). Such high cyclability is also superior to most graphene-coated micron-Si anodes and even some of nano-Si anodes (Fig. S11a). Moreover, a dramatic increase in the Coulombic efficiency was observed for the Si@Li-Si-O@rGO anode upon cycling (Fig. 4d), indicating remarkably improved reversibility and cyclability. The rate capability was also improved and the specific capacity was measured to be 1377, 1137, 905 and 703 mAh g^{-1} at 0.3, 0.5, 2 and 5 A g^{-1}, respectively (Fig. 4e). These values are comparable to and even better than those of reported high-graphene-modified Si anodes, especially at 5 A g^{-1} (Fig. S11b). It is worth highlighting that a highly stable long-term cyclability was also obtained at high current density. When cycled at 0.5 A g^{-1}, as shown in Fig. 4f, a high reversible capacity

of 962 mAh g^{-1} was obtained in the 310th cycle, corresponding to 97.7% of the 2nd cycle (985 mAh g^{-1}), remarkably better than that of Si@n-SiO_2/C reported recently (800.7 mAh g^{-1} after 300 cycles) [33]. Furthermore, no appreciable changes in the electrochemical properties were observed after rolling the Si@Li-Si-O@rGO wafer electrode (Fig. S12), exhibiting good flexibility at certain extent.

To understand the important roles played by hierarchical conformal coating, we further prepared three samples composed of Si/SiO_x, Si/rGO and Si/SiO_x/rGO, by directly mechanical milling Si under O_2 (Si/SiO_x) and combing pristine Si and Si/SiO_x with rGO through an identical encapsulation process described above, respectively. Severe pulverization (Fig. 5a) and amorphization (Fig. S13) were observed for the Si/SiO_x sample, and the average particle size was reduced to 0.4 μm after ball milling. Unlike the Si@Li-Si-O sample, coating was not achieved by milling Si under O_2 because both Si nanoparticles and fully oxidized SiO_x submicron particles in isolated states were distinguished by the EDS mapping analysis (Fig. 5b). This can be attributed to the poor mechanical properties of Si and amorphous SiO_x, which leads to continuous fracturing and pulverization during mechanical milling. This is further confirmed by measuring their elastic moduli and hardness values using nanoindentation technique. As shown in Fig. 5c-e, the elastic modulus and hardness of the pristine Si and Si/SiO_x are only 9.2/0.33 and 5.4/0.13 GPa, respectively. These values are increased to 31.8/1.29 GPa for Si@Li-Si-O obtained after 12 h milling. The enhanced mechanical properties are also responsible for the preservation of micron sized particles in the prepared Si@Li-Si-O particle (Fig. 2d-g).

Electrochemical measurements indicated nearly no improvement for the Si/SiO_x sample (Fig. S14) compared with Si, although the particle size was largely reduced (Fig. 5a). We therefore believe that the *in situ* formed Li-Si-O conformal coating layer enhances mechanical properties and anti-pulverization ability of the Si microparticles during lithiation/delithiation, which is in good agreement with our previous report [38,52]. SEM observation displayed good

integrity for as-fabricated pristine Si, Si@Li-Si-O and Si@Li-Si-O@rGO electrodes although there were some small cracks and even cavities on the surface (Fig. 6a-c). However, a remarkable change on the surface morphology was observed after 100 cycles (Fig. 6d-f). In contrast to the pristine Si electrode, where extensive fracturing was observed after 100 cycles (Fig. 6d), only large and deep cracks appeared on the surface of Si@Li-Si-O electrodes (Fig. 6e). This situation was further improved by encapsulating Si@Li-Si-O in graphene, which helps to buffer the volume change and therefore suppress the active materials from separation [53]. As a result, the Si@Li-Si-O@rGO electrode exhibited the best mechanical integrity with only a few cracks (Fig. 6f), consequently delivering the best cycling stability. However, it is difficult to encapsulate the pristine Si particles with rGO (Fig. S15). As for the Si/SiO_x mixture, even though the encapsulation structure can be formed, its quality is not high (Fig. S16), possibly due to the relatively weaker interaction between SiO_x with GO, as indicated by theoretical calculations, which offer a smaller adsorption energy while adsorbing SiO_x clusters on the GO surface (Fig. S17). This is responsible for their poor cycling stability. Furthermore, the comparison of zeta potential reveals that the presence of the Li-Si-O surface layer largely increased the surface charge of Si microparticles, evidenced by a twofold increase in zetal potential from 24.6 to 53.3 mV (Fig. S18) [54]. After PEI treatment, Li-Si-O surface became highly positively charged, which enables strong electrostatic interaction with negatively charged GO, leading to strong encapsulation by rGO after thermal annealing [55].

EIS examinations were conducted for pristine Si, Si@Li-Si-O and Si@Li-Si-O@rGO anodes after different charge/discharge cycles (Fig. 6g-i). The results were fitted with a frequently used equivalent circuit shown in Fig. S19 and summarized in Table 1. The fitting results exhibit a distinct increase in the SEI resistance (R_{sei}) and the surface electrochemical reaction resistance (R_{ct}) for the pristine Si with cycling, nearly 10-fold increase in the R_{ct} value after 100 cycles. This is mainly attributed to the poor electrical contact caused by severe pulverization and the continuous formation of unstable SEI film, as extensively reported

previously [29,30]. The increments in R_{sei} and R_{ct} are largely decreased for the Si@Li-Si-O (Fig. 6h) and Si@Li-Si-O@rGO (Fig. 6i) samples, due to the remarkably increased mechanical and chemical stability caused by the surface conformal coating, as discussed above. In addition, the encapsulation by graphene enhances electronic conductivity, which is also favourable for the reduction in the R_{ct} value (Table 1).

Moreover, the diffusion coefficient of Li^+ ion (D_{Li}) was calculated by fitting the EIS data (Fig. 7). For Si@Li-Si-O, the D_{Li} value is determined to be approximately 2.03×10^{-10} cm^2 s^{-1}, which is an order of magnitude higher than that of the pristine Si (3.97×10^{-11} cm^2 s^{-1}) and Si/SiO_x (2.04×10^{-11} cm^2 s^{-1}). This is mainly ascribed to the presence of nanocrystalline Li_2SiO_3 with high Li^+ conductivity in the SiO_x coating layer [56,57]. The highly conductive graphene and two-dimensional pancake-like morphology also contribute to high ion and electron transfer capability. In addition, the hierarchical conformal coating of Si microparticles enhances the mechanical and chemical stability and therefore facilitates the electron and ion transfer. All these factors contribute to the observed superior overall electrochemical properties of Si@Li-Si-O@rGO (Fig. 4e and f). Furthermore, the full cells were fabricated by pairing with home-made $Li_{1.2}Ni_{0.13}Co_{0.13}Mn_{0.54}O_2$ (LNCMO) cathode. The electrochemical performance was preliminarily evaluated at 2.5 - 4.2 V of potential window, which delivered 1092 mAh g^{-1} of specific capacity based on the mass loading of anode active materials, along with relatively stable cyclability (Fig. 8). More importantly, the Si@Li-Si-O@rGO||LNCMO full cell readily powered a green LED bulb working at 3 V as shown in the inset of Fig. 8b, showing a good possibility for practical applications.

4. Conclusion

In summary, a unique pancake-like microsized Si composite anode with the hierarchical conformal coating was fabricated through a facile reactive mechanical milling followed by

electrostatic self-assembly of rGO. The reactive mechanical milling generated a nanocrystalline Li_2SiO_3-embeded amorphous SiO_x conformal coating layer on the surface of Si microparticles, and the electrostatic self-assembly enabled a good encapsulation by graphene. This hierarchical conformal coating enhances the mechanical and chemical stability and facilitates the electron and ion transfer, consequently enhancing electrochemical performance. The elastic modulus and the diffusion coefficient of Li^+ ion were largely increased to 31.8 GPa and 2.03×10^{-10} cm^2 s^{-1}, respectively. As a result, the specific electrochemical capacity of the resulting Si@Li-Si-O@rGO composite was measured to be 1450 mAh g^{-1} at 0.1 A g^{-1}, and remained at 1258 mAh g^{-1} after 100 cycles. Moreover, the rate capability was also improved remarkably because the measured specific capacity was 703 mAh g^{-1} even operating at 5 A g^{-1}. In particular, the capacity retention as high as 97.7% was achieved from the 2nd to the 310th cycle while cycling at 0.5 A g^{-1}. Our findings reported in this work provide a new avenue for the rational design of microsized Si anodes for practical applications in high-performance Li-ion batteries.

CRediT authorship contribution statement

Yaxiong Yang: Conceptualization, Formal analysis, Investigation, Writing-original draft; **Shugang Liu**: Investigation, Visualization; **Zhe Dong**: Investigation, Visualization; **Zhenguo Huang**: Formal analysis, Writing - review & editing; **Cheng Lu**: Investigation, Visualization; **Yongjun Wu**: Conceptualization, Formal analysis; **Mingxia Gao**: Formal analysis, Methodology; **Yongfeng Liu**: Supervision, Conceptualization, Methodology, Resources, Project administration, Writing - review & editing; **Hongge Pan**: Supervision, Project administration, Conceptualization, Resources.

Acknowledgements

We gratefully acknowledge the financial support from the National Natural Science Foundation of China (51901168, 52071285 and 51831009), the National Outstanding Youth Foundation of China (52125104), the Fundamental Research Funds for the Central Universities (2021FZZX001-09), the National Youth Top-Notch Talent Support Program, the Natural Science Basic Research Plan in Shaanxi Province of China (2020JQ-809) and the Young Talent fund of University Association for Science and Technology in Shaanxi, China (20200428).

Appendix A. Supplementary data

Supplementary data associated with this article can be found, in the online version, at DOI.

References

[1] J. M. Tarascon, M. Armand, Issues and challenges facing rechargeable lithium batteries, Nature 414 (2001) 359-367. https://doi.org/10.1142/9789814317665_0024.

[2] B. Dunn, H. Kamath, J. M. Tarascon, Electrical Energy Storage for the Grid: A Battery of Choices, Science 334 (2011) 928-935. DOI: 10.1126/science.1212741.

[3] K. Turcheniuk, D. Bondarev, G. G. Amatucci, G. Yushin, Battery materials for low-cost electric transportation, Mater. Today 42 (2021) 57-72. https://doi.org/10.1016/j.mattod.2020.09.027.

[4] D. T. Ma, Y. L. Li, H. W. Mi, S. Luo, P. X. Zhang, Z. Q. Lin, J. Q. Li, H. Zhang, Robust SnO_{2-x} Nanoparticle-Impregnated Carbon Nanofibers with Outstanding Electrochemical Performance for Advanced Sodium-Ion Batteries, Angew. Chem. Int. Ed. 57 (2018) 8901 - 8905. https://doi.org/10.1002/anie.201802672.

[5] M. Qiu, Z. T. Sun, D. K. Sang, X. G. Han, H. Zhang, C. M. Niu, Current progress in black phosphorus materials and their applications in electrochemical energy storage, Nanoscale 9 (2017) 13384 - 13403. https://doi.org/10.1039/C7NR03318D.

[6] X. H. Chen, G. H. Xu, X. H. Ren, Z. J. Li, X. Qi, K. Huang, H. Zhang, Z. Y. Huang, J. X. Zhong, A black/red phosphorus hybrid as an electrode material for high-performance Li-ion batteries and supercapacitors, J. Mater. Chem. A 5 (2017) 6581 - 6588. https://doi.org/10.1039/C7TA00455A.

[7] D. T. Ma, Y. L. Li, J. B. Yang, H. W. Mi, S. Luo, L. B. Deng, C. Y. Yan, M. Rauf, P. X. Zhang, X. L. Sun, X. Z. Ren, J. Q. Li, H. Zhang, New Strategy for Polysulfide Protection Based on Atomic Layer Deposition of TiO_2 onto Ferroelectric-Encapsulated Cathode: Toward Ultrastable Free-Standing Room Temperature Sodium-Sulfur Batteries, Adv. Funct. Mater. 28 (2018) 1705537. https://doi.org/10.1002/adfm.201705537.

[8] B. Cao, H. Liu, P. Zhang, N. Sun, B. Zheng, Y. Li, H. L. Du, B. Xu, Flexible MXene Framework as a Fast Electron/Potassium-Ion Dual-Function Conductor Boosting Stable Potassium Storage in Graphite Electrodes, Adv. Funct. Mater. 31 (2021) 2102126. https://doi.org/10.1002/adfm.202102126.

[9] H. Liu, H. L. Du, W. Zhao, X. J. Qiang, B. Zheng, Y. Li, B. Cao, Fast potassium migration in mesoporous carbon with ultrathin framework boosting superior rate performance for high-power potassium storage, Energy Storage Mater. 40 (2021) 490 - 498. https://doi.org/10.1016/j.ensm.2021.05.037.

[10] M. Li, J. Lu, Z. W. Chen, K. Amine, 30 Years of Lithium-Ion Batteries, Adv. Mater. 30 (2018) 1800561. https://doi.org/10.1002/adma.201800561.

[11] Z. W. Liang, S. B. Li, B. Yuan, R. Z. Hu, J. Liu, M. Zhu, Reversible formation of metastable Sn-rich solid solution in SnO_2-based anode for high-performance lithium storage, App. Mater. Today 25 (2021) 101242. https://doi.org/10.1016/j.apmt.2021.101242.

[12] G.J. Zhu, D.L Chao, W.L Xu, M.H. Wu, H.J. Zhang. Microscale Silicon-Based Anodes: Fundamental Understanding and Industrial Prospects for Practical High-Energy Lithium-Ion Batteries. ACS Nano. (2021) DOI: 10.1021/acsnano.1c05898.

[13] H. Kim, E.-J. Lee, Y.-K. Sun, Recent advances in the Si-based nanocomposite materials as

high capacity anode materials for lithium ion batteries, Mater. Today 17 (2014) 285-297. http://dx.doi.org/10.1016/j.mattod.2014.05.003.

[14] W. Wei, K. Xu, N. Liao, W. Xue, Insight into Si/SiCO thin films anodes for lithium-ion batteries with high capacity and cycling stability, App. Mater. Today 20 (2020) 100773. https://doi.org/10.1016/j.apmt.2020.100773.

[15] M. T. McDowell, I. Ryu, S. W. Lee, C. M. Wang, W. D. Nix, Y. Cui, Studying the Kinetics of Crystalline Silicon Nanoparticle Lithiation with In Situ Transmission Electron Microscopy, Adv. Mater. 24 (2012) 6034-6041. https://doi.org/10.1002/adma.201202744.

[16] J. W. Wang, Y. He, F. F. Fan, X. H. Liu, S. M. Xia, Y. Liu, C. T. Harris, H. Li, J. Y. Huang, S. X. Mao, T. Zhu, Two-Phase Electrochemical Lithiation in Amorphous Silicon, Nano Lett. 13 (2013) 709-715. https://doi.org/10.1021/nl304379k.

[17] X. H. Liu, L. Zhong, S. Huang, S. X. Mao, T. Zhu, J. Y. Huang, Size-Dependent Fracture of Silicon Nanoparticles During Lithiation, ACS Nano. 6 (2012) 1522-1531. https://doi.org/10.1021/nn204476h.

[18] [12] M.-S. Wang, G.-L. Wang, S. Wang, J. Zhang, J. Wang, W. Zhong, In situ catalytic growth 3d multi-layers graphene sheets coated nano-silicon anode for high performance lithium-ion batteries. Chem. Eng. J. 356 (2019) 895-903. https://doi.org/10.1016/j.cej.2018.09.110

[19] Y. Yang, W. Yuan, W. Q. Kang, Y. Ye, Y. H. Yuan, Z. Q. Qiu, C. Wang, X. Q. Zhang, Y. Z. Ke, Y. Tang, Silicon-nanoparticle-based composites for advanced lithium-ion battery anodes, Nanoscale 12 (2020) 7461-7484. https://doi.org/10.1039/C9NR10652A.

[20] Y. Son, S. Sim, H. Ma, M. Choi. Y. Son, N. Park, J. Cho, M. Park, Exploring Critical Factors Affecting Strain Distribution in 1D Silicon-Based Nanostructures for Lithium-Ion Battery Anodes. Adv. Mater. 30 (2018) 1705430. https://doi.org/10.1002/adma.201705430.

[21] R. Yi, M.L. Gordin, D.H. Wang, Integrating Si nanoscale building blocks into micro-sized materials to enable practical applications in lithium-ion batteries, Nanoscale 8 (2016) 1834-

1848. https://doi.org/10.1039/C5NR07625K.

[22] P. N. Nie, Z. Y. Le, G. Chen, D. Liu, X. Y. Liu, H. B. Wu, P. C. Xu, X. R. Lu, F. Liu, L. M. Chang, X. G. Zhang, Y. F. Lu, Graphene caging silicon particles for high-performance lithium-ion batteries, Small 14 (2018) 1800635. https://doi.org/10.1002/smll.201800635.

[23] B. Lee, T. Y. Liu, S. K. Kim, H. Chang, K. Eom, L. X. Xie, S. Chen, H. D. Jang, S. W. Lee, Submicron silicon encapsulated with graphene and carbon as a scalable anode for lithium-ion batteries, Carbon 119 (2017) 438-445. https://doi.org/10.1016/j.carbon.2017.04.065.

[24] J. Müller, M. Abdollahifar, A. Vinograd, M. Nöske, C. Nowak, S. J. Chang, T. Placke, W. Haselrieder, M. Winter, A. Kwade, N. L. Wu, Si-on-graphite fabricated by fluidized bed process for high-capacity anodes of Li-ion batteries, Chem. Eng. J. 407 (2020) 126603. https://doi.org/10.1016/j.cej.2020.126603.

[25] A. Su, J. Li, J. J. Dong, D. Yang, G. Chen, Y. J. Wei, An Amorphous/Crystalline Incorporated Si/SiO_x Anode Material Derived from Biomass Corn Leaves for Lithium-Ion Batteries, Small 16 (2020) 2001714. https://doi.org/10.1002/smll.202001714.

[26] F. L. Wang, G. Chen, N. Zhang, X. H. Liu, R. Z. Ma, Engineering of carbon and other protective coating layers for stabilizing silicon anode materials, Carbon Energy 1 (2019) 219–245. https://doi.org/10.1002/cey2.24.

[27] E. Park, H. Yoo, J. Lee, M. S. Park, Y. J. Kim, H. Kim, Dual-size silicon nanocrystal-embedded SiO_x nanocomposite as a high-capacity lithium storage material, ACS Nano. 9 (2015) 7690-7696. https://doi.org/10.1021/acsnano.5b03166.

[28] B. Jiang, S. Zeng, H. Wang, D. T. Liu, J. F. Qian, Y. L. Cao, H. X. Yang, X. P. Ai, Dual Core−Shell Structured Si@SiO_x@C Nanocomposite Synthesizedvia a One-Step Pyrolysis Method as a Highly Stable Anode Materialfor Lithium-Ion Batteries, ACS Appl. Mater. Interfaces 8 (2016) 31611–31616. https://doi.org/10.1021/acsami.6b09775.

[29] L. Z. Guo, H. Y. He, Y. Ren, C. Wang, M. Q. Li, Core-shell SiO@F-doped C composites with interspaces and voids as anodes for high-performance lithium-ion batteries, Chem.

Eng. J. 335 (2018) 32-40. https://doi.org/10.1016/j.cej.2017.10.145.

[30] M. S. Wang, G. L. Wang, S. Wang, J. Zhang, J. Wang, W. Zhong, F. Tang, Z. L. Yang, J. M. Zheng, X. Li, In situ catalytic growth 3D multi-layers graphene sheets coated nano-silicon anode for high performance lithium-ion batteries, Chem. Eng. J. 356 (2019) 895-903. https://doi.org/10.1016/j.cej.2018.09.110.

[31] Z. Q. Gu, C. Liu, R. Y. Fan, Z. Zhou, Y. X. Chen, Y. D. He, X. H. Xia, Z. Y. Wang, H. B. Liu, Double core-shell of Si@PANI@TiO_2 nanocomposite as anode for lithium-ion batteries with enhanced electrochemical performance, Int. J. Hydrog. Energy 43 (2018) 20843-20852. https://doi.org/10.1016/j.ijhydene.2018.09.105.

[32] X. Y. Luo, J. L. Lang, S. S. Lv, Z. C. Li, High performance sandwich structured si thin film anodes with LiPON coating, Front. Mater. Sci. 12 (2018) 1-9. https://doi.org/10.1007/s11706-018-0416-1.

[33] X. Q. Dai, H. T. Liu, X. Liu, Z. L. Liu, Y. S. Liu, Y. H.. Cao, J. Y. Tao, Z. Q. Shan, Silicon nanoparticles encapsulated in multifunctional crosslinked nano-silica/carbon hybrid matrix as a high-performance anode for Li-ion batteries. Chem. Eng. J. 418 (2021) 129468. https://doi.org/10.1016/j.cej.2021.129468.

[34] H. T. Liu, X. Liu, Z. L. Liu, J. Y. Tao, X. Q. Dai, Q. Yang, J. K. Xu, Z. Q. Shan, Graphite@silicon embedded in a carbon conformally coated tiny SiO_2 nanoparticle matrix for high-performance lithium-ion batteries, Inorg. Chem. Front. 8 (2021) 4395. https://doi.org/10.1039/d1qi00618e

[35] Y. Xu, C. Stetson, K. Wood, E. Sivonxay, C. S. Jiang, G. Teeter, S. Pylypenko, S. D. Han, K. A. Persson, A. Burrell, Mechanical Properties and Chemical Reactivity of Li_xSiO_y Thin Films, ACS Appl. Mater. Interfaces 10 (2018) 38558-38564. https://doi.org/10.1021/acsami.8b10895.

[36] Y. K. Wang, Q. L. Zhang, D. W. Li, J. Z. Hu, J. G. Xu, D. Y. Dang, X. C. Xiao, Y. T. Cheng, Mechanical Property Evolution of Silicon Composite Electrodes Studied by Environmental

Nanoindentation, Adv. Energy Mater. 8 (2018) 1702578. https://doi.org/10.1002/aenm.201702578.

[37] M. T. McDowell, S. W. Lee, I. Ryu, H. Wu, W. D. Nix, J. W. Choi, Y. Cui, Novel Size and Surface Oxide Effects in Silicon Nanowires as Lithium Battery Anodes, Nano Lett. 11 (2011) 4018-4025. https://doi.org/10.1021/nl202630n.

[38] Y. X. Yang, C. L. Ni, M. X. Gao, J. W. Wang, Y. F. Liu, H. G. Pan, Dispersion- strengthened microparticle silicon composite with high anti-pulverization capability for Li-ion batteries, Energy Storage Mater. 14 (2018) 279-288. https://doi.org/10.1016/j.ensm.2018.04.008.

[39] Z. Yi, N. Lin, T. Xu, TiO_2 coated Si/C interconnected microsphere with stable framework and interface for high-rate lithium storage. Chem. Eng. J. 347 (2018) 214-222. https://doi.org/10.1016/j.cej.2018.04.101

[40] C. Liu, Q. Xia, C. Liao, S. P. Wu, Pseudocapacitance Contribution to Three-dimensional Micro-sized Silicon@Fe_3O_4@Few-layered graphene for High-rate and Long-life Lithium ion Batteries. Mater. Today Commun. 18 (2018) 66-73. https://doi.org/10.1016/j.mtcomm.2018.11.004.

[41] X. Zhang, T. Fang, Y. Gao, L. Liao, T. Ma, S. Gao, M. Wang, Dual-functionalized coating engineering toward buffering mechanical stress of the Si anode. Mater. Today Energy 18 (2020) 100561. https://doi.org/10.1016/j.mtener.2020.100561.

[42] K. Wang, Y. Tan, P. T. Li, B. Xue, J. M. Sun, Facile synthesis of double-layer-constrained microsized porous Si/SiO_2/C composites for lithium-ion battery anodes. ACS Appl. Mater. Interfaces 11 (2019) 37732-37740. https://doi.org/10.1021/acsami.9b12596.

[43] W. S. Chang, C. M. Park, J. H. Kim, Y. U. Kim, G. Jeong, H. J. Sohn, Quartz (SiO_2): a new energy storage anode material for Li-ion batteries, Energy Environ. Sci. 5 (2012) 6895-6899. https://doi.org/10.1039/C2EE00003B.

[44] M. S. Park, E. Park, J. Lee, G. Jeong, K. J. Kim, J. H. Kim, Y. J. Kim, H. Kim, Hydrogen Silsequioxane-Derived Si/SiO_x Nanospheres for High-Capacity Lithium Storage Materials,

ACS Appl. Mater. Interfaces 6 (2014) 9608-9613. https://doi.org/10.1021/am5019429.

[45] J. Li, J. R. Dahn, J. Electrochem, An in Situ X-ray Diffraction Study of the Reaction of Li with Crystalline Si, J. Electrochem. Soc. 154 (2007) A156-A161. https://doi.org/10.1149/1.2409862.

[46] L. A. Berla, S. W. Lee, Y. Cui, W. D. Nix, Mechanical behavior of electrochemically lithiated silicon, J. Power Sources 273 (2015) 41-51. https://doi.org/10.1016/j.jpowsour.2014.09.073.

[47] G. Z. Li, B. Huang, Z. F. Pan, X. Y. Su, Z. P. Shao, L. An, Advances in three-dimensional graphene-based materials: configurations, preparation and application in secondary metal (Li, Na, K, Mg, Al)-ion batteries, Energy Environ. Sci. 12 (2019) 2030-2053. https://doi.org/10.1039/C8EE03014F.

[48] X. S. Zhou, Y. X. Yin, L. J. Wan, Y. G. Guo, Self-assembled nanocomposite of silicon nanoparticles encapsulated in graphene through electrostatic attraction for lithium-ion batteries, Adv. Energy Mater. 2 (2012) 1086-1090. https://doi.org/10.1002/aenm.201200158.

[49] D. A. Agyeman, K. Song, G. H. Lee, M. Park, Y. M. Kang, Carbon-coated si nanoparticles anchored between reduced graphene oxides as an extremely reversible anode material for high energy-density Li-ion battery, Adv. Energy Mater. 6 (2016) 1600904. https://doi.org/10.1002/aenm.201600904.

[50] D. X. Yang, A. Velamakanni, G. Bozoklu, S. Park, M. Stoller, R. D. Piner, S. Stankovich, I. Jung, D. A. Field, C. A. VentriceJr, R. S. Ruoff, Chemical analysis of graphene oxide films after heat and chemical treatments by X-ray photoelectron and Micro-Raman spectroscopy, Carbon 47 (2009) 145-152. https://doi.org/10.1016/j.carbon.2008.09.045.

[51] X. Cai, W. Liu, Z. Q. Zhao, S. M. Li, S. Y. Yang, S. S. Zhang, Q. Z. Gao, X. Y. Yu, H. Q. Wang, Y. P. Fang, Simultaneous encapsulation of nano-Si in redox assembled rGO film as binder-free anode for flexible/bendable lithium-ion batteries, ACS Appl. Mater. Interfaces

11 (2019) 3897–3908. https://doi.org/10.1021/acsami.8b18134.

[52] Y. X. Yang, X. L. Qu，L. C. Zhang, M. X. Gao, Y. F. Liu, H. G. Pan, A reaction-ball-milling-driven surface coating strategy to suppress pulverization of microparticle Si anodes, ACS Appl. Mater. Interfaces 10 (2018) 20591-20598. https://doi.org/10.1021/acsami.8b05609.

[53] C. H. Huang, Z. J. Feng, F. Pei, A. Fu, B. H. Qu, X. Y. Chen, X. L. Fang, H. Z. Kang, J. Q. Cui, Understanding Protection Mechanisms of Graphene-Encapsulated Silicon Anodes with Operando Raman Spectroscopy, ACS Appl. Mater. Interfaces 12 (2020) 35532−35541. https://doi.org/10.1021/acsami.0c03559.

[54] K. A. Hays, B. L. Armstrong, G. Veith, Ending the chase for a perfect binder: role of surface chemistry variation and its influence on silicon anodes, ChemElectroChem 7 (2020). https://doi.org/10.1002/celc.202001066.

[55] G. R. Zheng, Y. X. Xiang, L. F. Xu, H. Luo, B. L. Wang, Y. Liu, X. Han, W. M. Zhao, S. J. Chen, H. L. Chen, Q. B. Zhang, T. Zhu, Y. Yang, Controlling surface oxides in Si/C nanocomposite anodes for high-performance li-ion batteries, Adv. Energy Mater. 8 (2018) 1801718. https://doi.org/10.1002/aenm.201801718.

[56] E. Y. Zhao, X. F. Liu, H. Zhao, X. L. Xiao, Z. B. Hu, Ion Conducting Li_2SiO_3-coated Lithium-rich Layered Oxide Exhibiting High Rate Capability and Low Polarization, Chem. Commun. 51 (2015) 9093-9096. https://doi.org/10.1039/C5CC00383K.

[57] J. I. Lee, Y. Ko, M. Shin, H. K. Song, N. S. Choi, M. G. Kim, S. Park, High-performance silicon-based multicomponent battery anodes produced via synergistic coupling of multifunctional coating layers, Energy Environ. Sci. 8 (2015) 2075-2084. DOI: 10.1039/C5EE01493J.

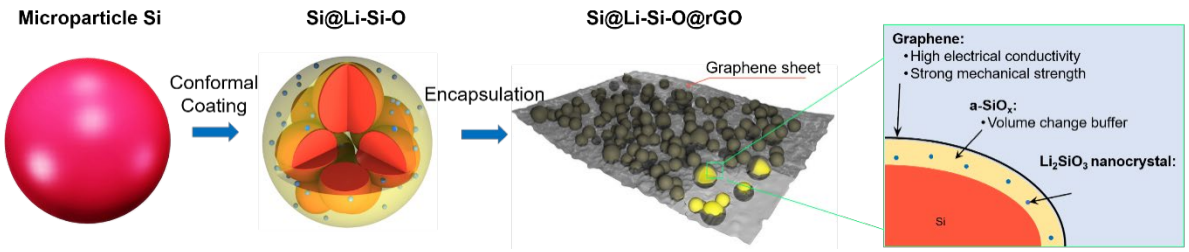

Fig. 1 Schematics of the preparation process and morphologic characteristics of the pancake-like micron-Si with hierarchical conformal coating.

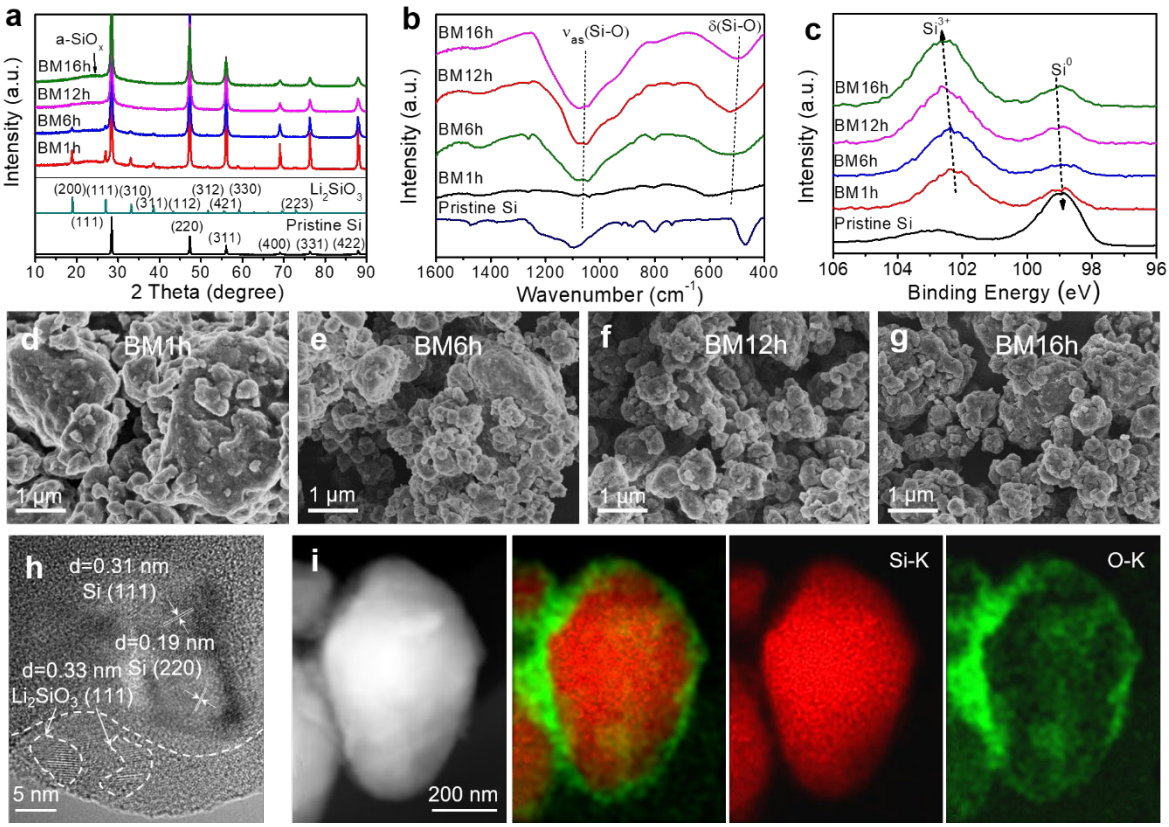

Fig. 2 (a) XRD patterns, (b) FTIR spectra, and (c) high resolution Si 2p XPS spectra of pristine Si microparticles and the prepared Si@Li-Si-O samples with different milling durations. (d-g) SEM images of as-milled samples. (h) HRTEM images of Si@Li-Si-O (BM12h). (i) STEM image of Si@Li-Si-O (BM12h) and corresponding EDS mapping of Si (red) and O (green).

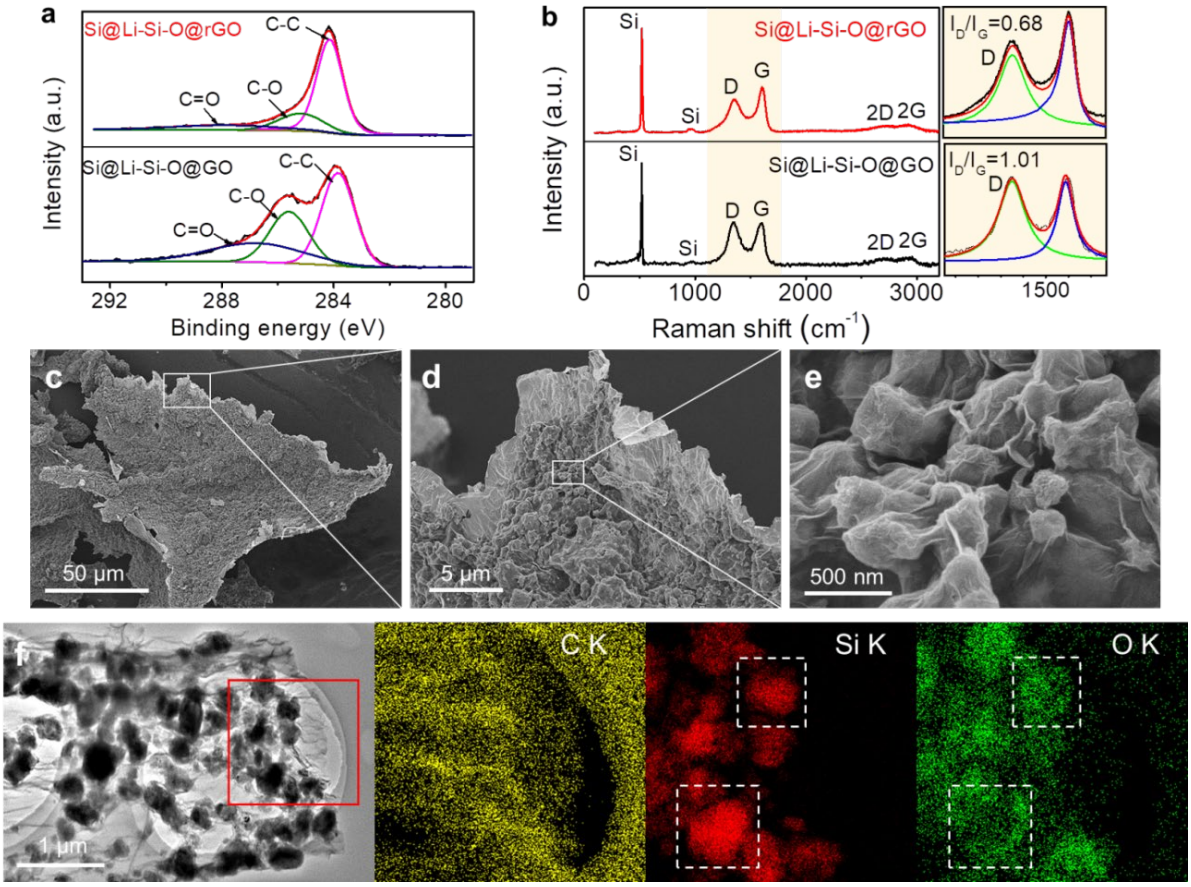

Fig. 3 (a) High-resolution C1s XPS, (b) Raman spectra, (c-e) SEM and (f) STEM and corresponding EDS mapping of the prepared Si@Li-Si-O@rGO.

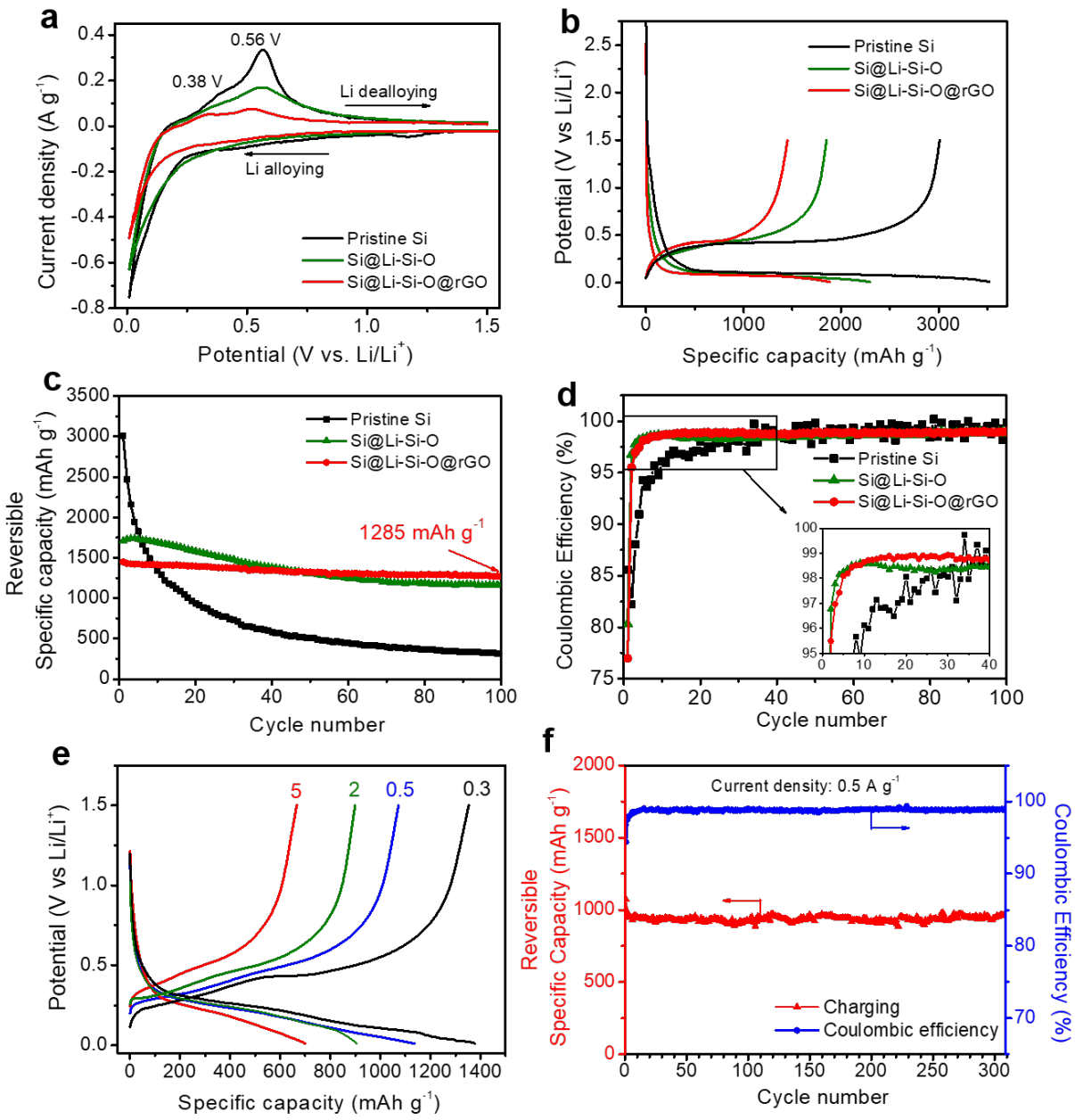

Fig. 4 (a) First CV curves, (b) first voltage profiles, (c) cycling performance measured at 0.1 A g^{-1} and (d) corresponding Coulombic efficiency (Inset: zoom in image) of the pristine Si, Si@Li-Si-O and Si@Li-Si-O@rGO anodes, (e) specific capacities of the Si@Li-Si-O@rGO anode measured at different current densities. (f) Cycling stability and corresponding Coulombic efficiency of the Si@Li-Si-O@rGO anode measured at 0.5 A g^{-1} during 310 cycles (the electrode was first activated at 0.1 A g^{-1}, which was not shown here).

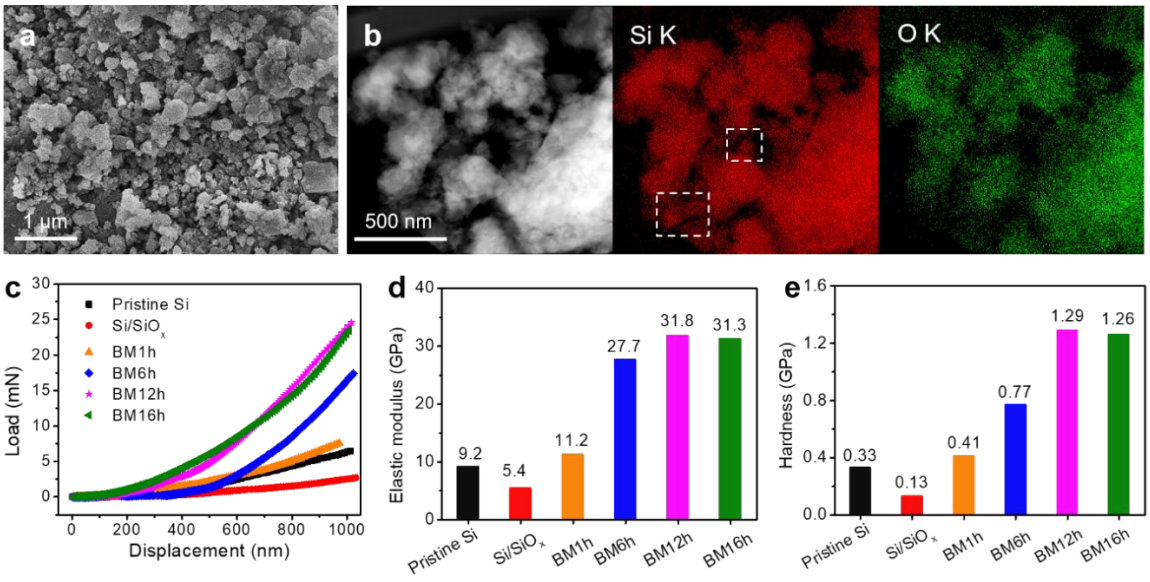

Fig. 5 (a) SEM image and (b) STEM and corresponding EDX mapping of the prepared Si/SiO_x. Some unoxidized Si nanoparticles were marked out by the dotted boxes. (c) Nanoindentation load/displacement curves, (d) elastic moduli and (e) hardness values measured for the pristine Si, Si/SiO_x and Si@Li-Si-O after different milling durations.

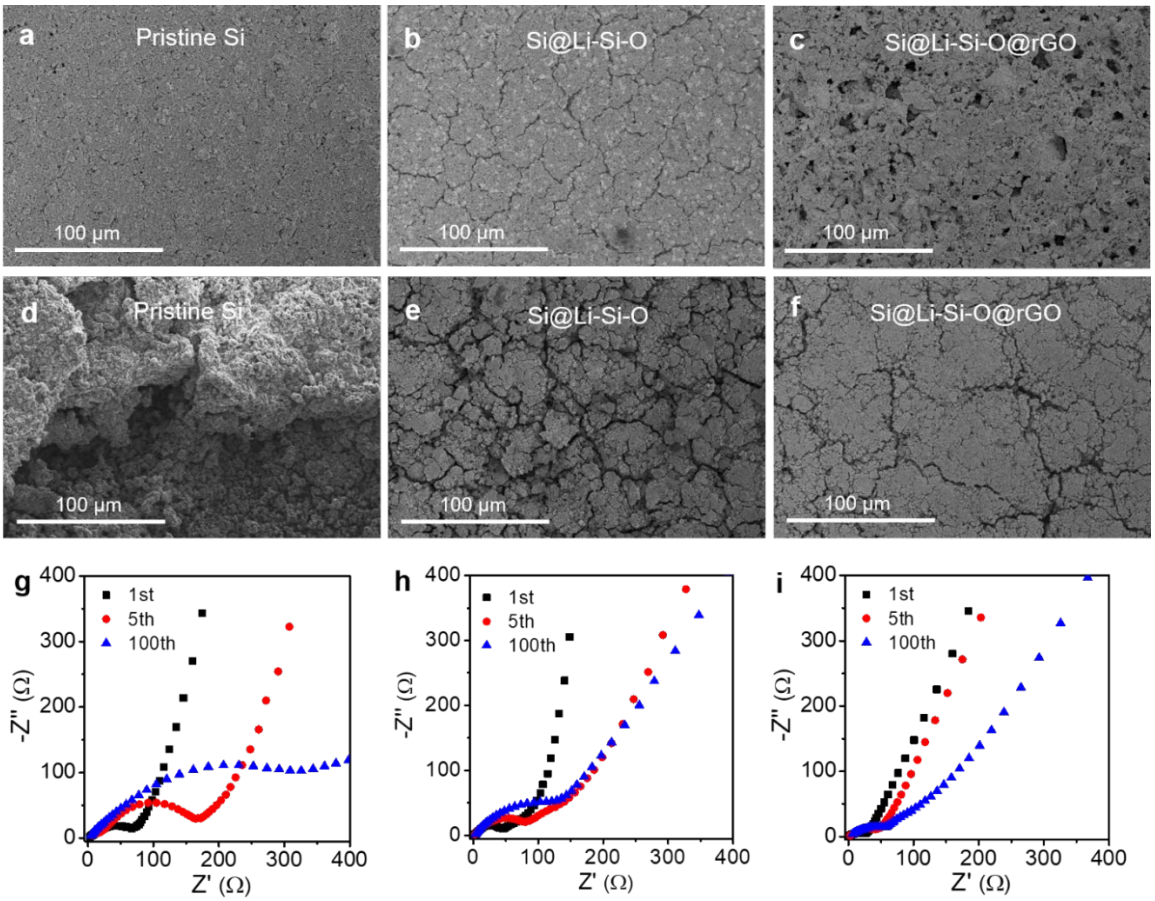

Fig. 6 SEM images of (a,d) pristine Si, (b,e) Si@Li-Si-O and (c,f) Si@Li-Si-O@rGO electrodes before (a-c) and after (d-f) 100 cycles. EIS spectra of (g) the pristine Si, (h) Si@Li-Si-O and (i) Si@Li-Si-O@rGO electrodes measured at different cycles.

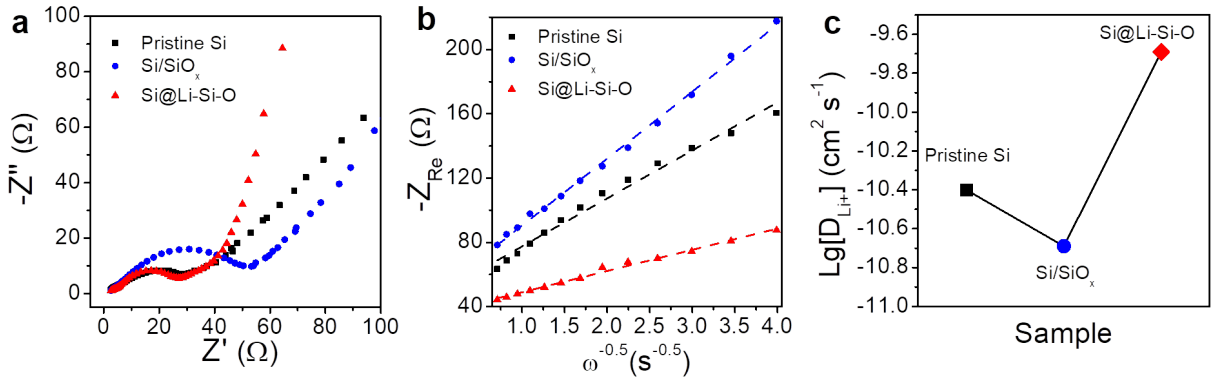

Fig. 7 (a) Nyquist plots, (b) plots of real impedance (Z_{Re}) against the reciprocal square root of the lower angular frequencies ($\omega^{-1/2}$) and (c) plot of diffusion coefficient values for Li^+ ions (D_{Li}) of pristine Si, Si/SiO_x and Si@Li-Si-O samples after 1 charge/discharge cycle.

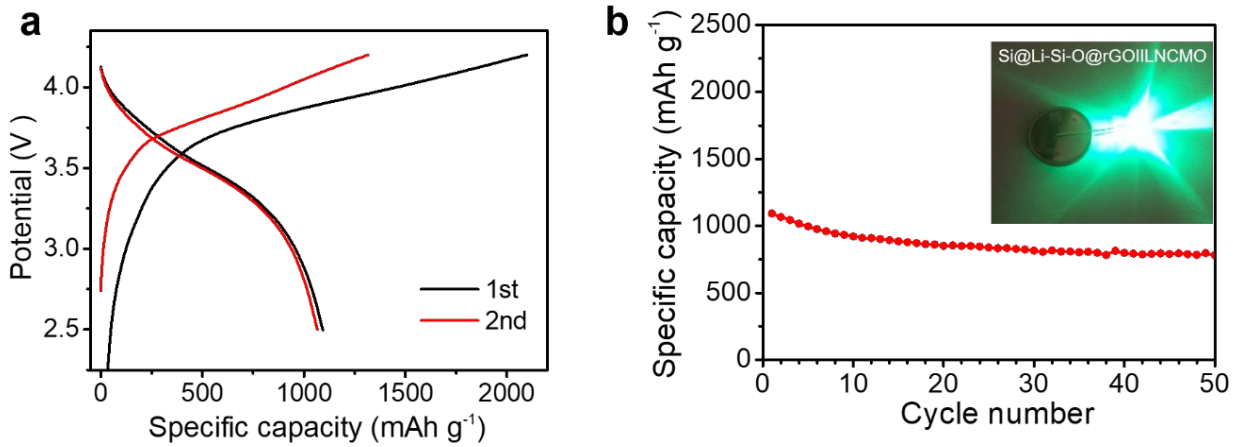

Fig. 8 (a) Charge-discharge curves and (b) cycling performance of Si@Li-Si-O@rGO||LNCMO full cell. Inset: a green LED bulb powered by the fabricated full cell.

Table 1 The calculated impedance values of the pristine Si, Si@Li-Si-O and Si@Li-Si-O@rGO electrodes at different cycles.

Cycles	R_{sei} (Ω)			R_{ct} (Ω)		
	Pristine Si	Si@Li-Si-O	Si@Li-Si-O@rGO	Pristine Si	Si@Li-Si-O	Si@Li-Si-O@rGO
1st	12.6	12.2	10.7	42.6	47.9	19.6
5th	37.1	30.7	12.7	154.9	96.5	32. 3
100th	88.1	34.7	25.0	420.3	216.6	61.9